submitted to The Astronomical Journal
Preprint typeset using LaTeX style emulateapj v. 14/09/00

ON THE OPTIMIZATION OF BROAD-BAND PHOTOMETRY FOR GALAXY EVOLUTION STUDIES

A. Gil de Paz[1,2] and B. F. Madore[1,3]
submitted to The Astronomical Journal

ABSTRACT

We have derived the uncertainties to be expected in the derivation of galaxy physical properties (star formation history, age, metallicity, reddening) when comparing broad-band photometry to the predictions of evolutionary synthesis models. We have obtained synthetic colors for a large sample (∼9000) of artificial galaxies assuming different star formation histories, ages, metallicities, reddening values, and redshifts. The colors derived have been perturbed by adopting different observing errors, and compared back to the evolutionary synthesis models grouped in different sets. The comparison has been performed using a combination of Monte Carlo simulations, a Maximum Likelihood Estimator and Principal Component Analysis. After comparing the input and derived output values we have been able to compute the uncertainties and covariant degeneracies between the galaxy physical properties as function of (1) the set of observables available, (2) the observing errors, and (3) the galaxy properties themselves. In this work we have considered different sets of observables, some of them including the standard Johnson/Cousins ($UBVR_CI_C$) and Sloan Digital Sky Survey (SDSS) bands in the optical, the 2 Micron All Sky Survey (2MASS) bands in the near-infrared, and the Galaxy Evolution Explorer (GALEX) bands in the UV, at three different redshifts, z=0.0, 0.7, and 1.4. This study is intended to represent a basic tool for the design of future projects on galaxy evolution, allowing an estimate of the optimal band-pass combinations and signal-to-noise ratios required for a given scientific objective.

Subject headings: galaxies: photometry – galaxies: evolution – methods: numerical – methods: statistical

1. introduction

The catalogs produced by wide-field and all-sky surveys currently under development (e.g., GALEX; Martin et al. 1997, SDSS; York et al. 2000, 2MASS; Skrutskie et al. 1997, DENIS; Epchtein et al. 1997) in combination with astronomical databases like the NASA/IPAC Extragalactic Database (NED) are beginning to provide easy access to extensive cross-correlated UV, optical, and near-infrared (NIR) photometry for millions of galaxies. The comparison of this huge amount of photometric data with the predictions of state-of-the-art galaxy population synthesis models provides an opportunity to obtain a more complete picture of the evolution of galaxies. One obvious goal is to gain insight into the star formation history, as well as the chemical and dust content evolution of galaxies from the high and intermediate redshift Universe down to the present.

However, the reliability and precision of the derived galaxy properties expected to be found from these studies will depend on many factors; among these are: (1) the number of bands and wavelength coverage of the available observations, (2) the measuring uncertainties, and (3) the degeneracies between the different galaxy properties given the available photometric bands. In order to discriminate between different scenarios of galaxy evolution, the comparison of photometric data and evolutionary synthesis models should also include the quantification of the uncertainties and covariances between the galaxy properties derived. In addition, the use of different external inputs (evolutionary tracks, stellar atmospheres libraries, etc.) in the evolutionary synthesis models leads to various discrepancies in the output results which may also result in significant uncertainties in the properties derived. While, a detailed study of these latter effects is beyond the scope of this paper, a nice approach to this problem may be found in Charlot, Worthey & Bressan (1996; see also Bruzual 2000, Cerviño, Luridiana & Castander 2000, Cerviño et al. 2001).

Some recent studies have incorporated the effects of the observing errors and flux calibration uncertainties in the determination of the properties of different galaxy samples (Gil de Paz et al. 2000a, GIL00a hereafter; Bell & de Jong 2000; Brinchmann & Ellis 2000). However, this type of analysis has not yet been performed in a systematic way, covering a large range of galaxy properties and/or star formation scenarios. A relevant exception is the work of Ronen, Aragon-Salamanca, & Lahav (1999) on the Principal Component Analysis of synthetic galaxy spectra. Similarly, no significant effort has yet been devoted to determining quantitatively the optimal set of observables and signal-to-noise ratio required to obtain reliably derived galaxy properties. Noteworthy exceptions are the works of Kodama, Bell & Bower (1999), Bolzonella, Miralles & Pello (2000), and Wolf, Meisenheimer & Roser (2001) with regard to the galaxy classification and redshift determination in broad and medium-band surveys.

In this paper we explore the uncertainties expected in the derived properties of galaxies obtained from the analysis of broad-band photometry of nearby, intermediate, and

[1] NASA/IPAC Extragalactic Database, California Institute of Technology, MS 100-22, Pasadena, CA 91125; agpaz, barry@ipac.caltech.edu
[2] Jet Propulsion Laboratory, MS 183-900, Pasadena, CA 91109
[3] The Observatories, Carnegie Institution of Washington, 813 Santa Barbara Street, Pasadena, CA 91101

high-redshift objects. We quantify these uncertainties using a sample of artificially generated spectral energy distributions (converted to broadband colors) with known (input) physical properties, studying the dependence of the properties derived with the sets of bands available, the observing errors, as well as the galaxy star formation history and redshift. This work has interesting predictive capabilities and is intended to help in the design of future projects on the study of galaxy evolution. It can be used in the optimization of observing programs, helping to select the best wavelength bands and signal-to-noise ratios required to derive precise galaxy properties. This contribution is mainly focused on the study of the integrated properties of galaxies, star clusters and H ii regions, although it is our intent to generalize the application to spatially resolved portions of galaxies as well. A similar approach has been followed by Charlot & Longhetti (2001) for the optimization of emission-line data in galaxy spectra, although no error analysis was carried out by those authors.

In the Section 2 of this paper we briefly describe the synthetic galaxy sample. The procedure followed for determining the uncertainties and degeneracies between the physical properties in this sample is described in Section 3. Section 4 includes a detailed description of the results from this analysis. The main conclusions are given in Section 5. Finally, some future applications for this work are given in Section 6.

2. the sample

We have generated a large number of synthetic galaxy colors parameterized by different star formation histories, metallicities, reddening, and redshifts. Because of the unbounded number of possible combinations we have made some choices and simplifications.

With regard to their star formation history we have considered galaxies with exponential star formation having timescales ( ) between 0.2 Gyr and 6 Gyr. Although this scenario is a rough approximation to the actual star formation histories it constitutes the most widely accepted parameterization of the star formation history in individual galaxies (see e.g. Brinchmann & Ellis 2000).

Thus, the properties to be determined are the timescale for the galaxy formation, the age of the galaxy, the stellar metallicity, and the reddening. A total of 9000 synthetic galaxies were generated, a third of them at redshift z=0.0, another third at z=0.7, and the remainder at redshift z=1.4. These redshift values were chosen to cover the epoch where most of the evolution of the star formation activity in the Universe has apparently taken place (Gallego et al. 1995; Madau et al. 1996; Connolly et al. 1997; Madau, Dickinson & Pozzetti 1998). Since the models available only provide discrete values in metallicity we chose to assign to each galaxy the nearest metallicity value of those given by the corresponding model. The ranges of physical properties covered by the galaxies in the sample are shown in Table 1.

Although a complete study about the effects of the model uncertainties on the galaxy properties derived is beyond the scope of this paper, the impact of the errors in the broad-band colors due to stellar evolution prescription and spectral calibration uncertainties (Charlot et al. 1996; Yi, Demarque & Oemler 1997) will be taken into account in our further analysis. In addition, in order to illustrate the effect of these uncertainties we have considered two different sets of evolutionary synthesis models. The synthetic galaxies were generated using the predictions for the stellar continuum given by the GISSEL99 models (Bruzual & Charlot, in preparation) while the best-fitting set of properties has been derived using both the GISSEL99 and the PEGASE models (Version 2.0; see Fioc & Rocca-Volmerange 1997). Although the theoretical isochrones in both models come mainly from the Padova group (Bressan et al. 1993), there are fundamental differences in post-main-sequence evolutionary stages between the two set of models, including in the early, thermally pulsating, and post-AGB phases. Noteworthy, the differences in these evolutionary stages are responsible for the most serious uncertainties in the stellar population modeling (see Charlot et al. 1996). In Figure 1 we show the predictions of these two models for Simple Stellar Population (SSP) and continuous star formation galaxies with Solar metallicity. For the sake of comparison we have also included the predictions of the Starburst 99 models (Leitherer et al. 1999) at ages younger than 0.1 Gyr.

3. analysis

3.1. Galaxy Colors

Once the sample was generated we determined the luminosity (per Solar mass) in the different bands and the colors for each individual galaxy in the sample using the predictions of the corresponding evolutionary synthesis models. We adopted for all the models the same Salpeter IMF with M_{low}=0.1M and M_{up}=100M .

The bands considered in this work include the Johnson/Cousins ($UBVR_C I_C$) and Sloan Digital Sky Survey $u^0g^0r^0i^0z^0$ (Fukugita et al. 1996) optical bands, the JHK near-infrared bands, and the GALEX near-ultraviolet (NUV, 1800–3000A) and far-ultraviolet bands (FUV, 1350–1800A; Doliber et al. 2000). Because of the small differences expected between the standard K-band and the K_s and K^0 bands, we decided to include only the standard K in our realizations. In this sense, although the 2MASS survey has been carried out using K_s-band imaging data, we will refer hereafter to the 2MASS data set when dealing with the standard JHK bands.

The colors obtained for each stellar population were then reddened (and the apparent mass-to-light ratios increased) using the corresponding E(B V) values and adopting the parameterization of the Galactic extinction law of Cardelli, Clayton & Mathis (1989) for a total-to-selective extinction ratio R_V=3.1. However, since this parameterization is only valid down to 1000A, and given that some of the bands selected for this work cover regions of galaxy spectra well below the Lyman limit (for z=0.7 and z=1.4), we extended the extinction law to the far-UV using the A /A_V ratios given by Mathis (1990; see also Martin & Rouleau 1989). The A /A_V mean values for each band (its respective redshifted rest-frame wavelength) were then computed convolving the filters response functions with the adopted extinction curve.

Using the number of ionizing Lyman photons predicted by the evolutionary synthesis models we also computed the contribution of the nebular continuum and most intense gas emission-lines to all the bands considered. We assumed that 85% of the photons with $\lambda < 912$Å effectively ionize the surrounding gas, but a 15 per cent fraction would be observed at the far-ultraviolet or absorbed by dust (Leitherer et al. 1995; Dove, Shull & Ferrara 2000; GIL00a).

Most of the 85% of the far-UV photons absorbed by the surrounding gas in the H ii region is reprocessed as nebular continuum and emission lines in the optical and NIR. However, a very small fraction of these photons can be re-emitted as free-free radiaton in the far-UV. In our case, we assumed that these secondary far-UV photons are not absorbed by neutral gas again, but rather being absorbed by dust or escaping from the galaxy. In order to determine the nebular continuum contribution to all the bands we have used the emission and recombination coefficients given by Ferland (1980) for the near-UV, optical, and NIR for $T_e = 10^4$ K. For the far-UV free-free radiation we have assumed a constant gaunt factor $\overline{g}_{ff} = 1.1$ (see Karzas & Latter 1961) in the range 500–912Å for a gas with $T_e = 10^4$ K.

With regard to the gas emission-lines we have assumed the relation between the number of Lyman photons and Hα luminosity given by Brocklehurst (1971) and the theoretical hydrogen line-ratios expected for a low density gas ($n_e = 10^2$ cm^{-3}) with $T_e = 10^4$ K in Case B recombination (Osterbrock 1989). We considered the contribution of the most intense forbidden lines ([O ii] $\lambda\lambda$3726,3729Å, [O iii] $\lambda\lambda$4959,5007Å, [N ii] $\lambda\lambda$6548,6583Å, [S ii] $\lambda\lambda$6717,6731Å) adopting the mean line ratios measured by Gallego et al. (1996) for the Universidad Complutense de Madrid (UCM) sample of local star-forming galaxies (Zamorano et al. 1994, 1996). Both the nebular continuum and the emission-line luminosities were corrected for extinction assuming the relation given by Calzetti, Kinney & Storchi-Bergmann (1996, see also Calzetti 1997; Storchi-Bergmann, Calzetti & Kinney 1994) between the gas and the stellar continuum reddening associated with the young stellar population: $E(B-V)_{stellar} = 0.44\ E(B-V)_{gas}$.

Following this procedure we obtain all the input information concerning the actual properties, colors, and mass-to-light ratios for the galaxies in the sample. In the next section we discuss our recovery of these input properties starting from the observed galaxy colors, and their corresponding measuring errors.

3.2. Sets of Colors

Grouping the colors deduced for these galaxies in different sets and comparing them with the evolutionary synthesis models allows us to explore systematics and determine the set of observables that result in minimum differences between the actual (input) galaxy properties and the derived (output) properties. This comparison is done using a combination of Monte Carlo simulations, a maximum likelihood estimator, and a Principal Component Analysis algorithm.

The number of different combinations of colors that could be constructed considering a total of 10 potential bands from the UV to the near-infrared is $\sum_{r=2}^{10}\frac{10!}{r!(10-r)!} = 1013$. For this study we have selected only the 10 sets shown in Table 2. The detailed comparison of the results obtained for all these sets provides enough information about the relevance of the different bands, observing errors, etc., for a precise determination of the galaxy properties.

3.3. Comparison Procedure

Once the colors of the galaxy sample had been obtained and grouped in sets we then perturbed the "observed" magnitudes by applying random observing errors. In order to simplify the problem we studied three cases, corresponding to three different 1-sigma errors in the colors, 0.03, 0.07, and 0.10 mag, and consider only the case where these errors are the same in all the colors.

In order to compute the effects of these observing errors in the galaxy properties to be derived we used a Gaussian distribution of errors for all bands generated using a Monte Carlo simulation method. The colors derived for each test-particle were then compared with the evolutionary synthesis models using a maximum likelihood estimator, L. The expression for this estimator (see e.g. Abraham et al. 1999) is

$$L = \prod_{n=1}^{N} \frac{1}{\sqrt{2\pi}\,\sigma_{C_n}} \exp\left(-\frac{(c_n - C_n)^2}{2\sigma_{C_n}^2}\right) \qquad (1)$$

where C_n are the colors derived, c_n are those predicted by the evolutionary synthesis models and N is the total number of colors available within each set. Because the same level of error was assumed for all the bands, the maximization of this expression is equivalent to computing the minimum χ^2. Therefore, in this case, we could estimate the confidence levels in the galaxy properties via the Avni's approximation (Avni 1976) as has been done by Bolzonella et al. (2000) instead of using numerical simulations. However, the considerations that lead to this estimation procedure apply only asymptotically, being applicable when the χ^2 estimator covariance matrix can be replaced by its linear approximation in the vicinity of the best-fitting set of parameters. Although these conditions could be fulfilled in our case (Perez-Gonzalez et al. 2001, in preparation), we have decided to use numerical simulations in order to be able to derive the degeneracies between the different galaxy properties.

The ranges in the evolutionary synthesis models parameters where the data-model comparison was performed are shown in Table 1. In order to avoid introducing a constraint bias in the derived properties, the ranges for these comparison were chosen to be significantly wider than those where the galaxy sample was generated.

Once the expression L is maximized for a significant number of Monte Carlo test-particles (we used a total of 200) we obtained the distribution of physical properties associated with the probability distribution of the galaxy colors. In Figures 2a, b & c we show the results obtained for a nearby galaxy with a exponential star formation history with $\tau = 4.5$ Gyr timescale, Solar metallicity, an age of 5.0 Gyr, and $E(B-V)$ of 0.08 mag, for observing errors in the colors of 0.10, 0.07, and 0.03 mag, respectively. In this case the set of colors used was that including the GALEX, SDSS, and 2MASS bands (see Table 2).

These figures illustrate the strong degeneracy between the different galaxy properties even for relatively small measurement errors. We have therefore performed a quantitative analysis of these degeneracies using a Principal

Component Analysis (PCA hereafter) on the space of galaxy properties by solving the eigenvector equation on the test-particle correlation matrix of each galaxy in the sample (see Morrison 1976). This analysis gives the direction in the space of galaxy properties along which the 200 solutions obtained for each individual galaxy are mainly oriented, constituting the best estimator of the degeneracy between these properties.

Summarizing, this procedure provides us with (1) the mean derived properties, (2) the 1-sigma errors, (3) the orientation in the space of solutions of the Principal Component (PCA1 hereafter), and (4) the input (i.e: actual) properties of all galaxies in the sample.

4. results

Once these quantities had been derived we computed the mean differences between the output and input values along with the mean 1-sigma spread, at fixed intervals in the input properties. The bins used were 0.5 Gyr, 0.025 dex, and 0.025 mag in the formation timescale, age, and reddening, respectively. Mean differences and 1-sigma values in the stellar metallicity were computed for each of the input values considered.

In Figures 3a & b we show the results obtained before and after computing the mean differences and 1-sigma errors for a subsample of 500 nearby galaxies with errors in the colors of 0.07 mag and U+BVRI+JHK data available. Due to the relevance of the K-band luminosities in order to derive stellar masses in nearby (Aragon-Salamanca et al. 1993; GIL00a) and intermediate-redshift galaxies (see Brinchmann & Ellis 2000 and references therein), the mean differences between the derived and input K-band mass-to-light ratios were also computed. Mean uncertainties for all the sets of observables, redshifts, and observing errors considered are summarized in Table 3.

In addition, we studied the degeneracies between the galaxy physical properties analyzing the distribution of the unitary PCA1 vector components. In Figure 4a we show the frequency histograms obtained for the sample of high-redshift galaxies assuming an error in the colors of 0.07 mag and the SDSS, SDSS+2MASS, and GALEX+SDSS+2MASS sets. Note that the PCA1 vector points toward the direction where the largest fraction of the galaxy properties' variance occurs. In this sense, a PCA1 vector with components ($u_{\log t}$,$u_{E(B-V)}$,$u_{\log Z=Z}$,u) = (+0.707, 0.707,0,0), say, implies the existence of a degeneracy between age and reddening in the sense that younger, obscured stellar populations have colors that are indistinguishable from older but less extincted ones. In this case, no age-metallicity or age-timescale degeneracies would be present. However, the behavior described above could also result in a PCA1 vector with components ($u_{\log t}$,$u_{E(B-V)}$,$u_{\log Z=Z}$,u) = (0.707,+0.707,0,0). That, however, would appear in a different position at the frequency histogram shown in Figure 4a. Thus, in order to reduce this sign ambiguity when interpreting our results we forced the $u_{\log t}$ component to be positive, changing the sign of all the vector components if $u_{\log t}$ was negative. Finally, in order to quantitatively determine the dominant degeneracy for each individual galaxy in our sample we have defined the angle $_{i;j}$ like that satisfying

$$\cos_{i;j} = \mathrm{SIGN}\left(\frac{u_i}{u_j}\right)\sqrt{u_i^2 + u_j^2} \qquad (2)$$

where u_i and u_j are the i and j components of the PCA1 vector. The angle $_{i;j}$ simultaneously provides a measure of the angle between the PCA1 vector and the plane of physical properties $i;j$ and the sign of the degeneracy between the i and j properties. Thus, if $|\cos_{i;j}| \simeq 1$ the degeneracy between the i and j properties would dominate the total degeneracy. Moreover, if $\cos_{i;j} > 0$ an increase in both the i and j properties would lead to similar observational properties, while if $\cos_{i;j} < 0$ the value of one of the properties should decrease. In Figure 4b we show the distribution of $\cos_{i;j}$ as function of the age for the high-redshift sample assuming an error in the colors of 0.07 mag and the GALEX+SDSS+2MASS set available.

Along this section we will describe the results obtained from the analysis of the distributions shown in Figures 3 & 4 for the different redshifts, observing errors, and band-pass combinations considered.

4.1. Nearby galaxies

4.1.1. Formation Timescale

With regard to the formation timescale in nearby galaxies, Figure 5a indicates that, even for relatively small observing errors, its uncertainty is very high (see also Table 3) and shows a strong dependence with the value of the formation timescale itself. The larger uncertainty in the formation timescale for larger values of this quantity is mainly due to the small sensitivity of the optical-NIR colors of stellar populations with ages $t <<$ to changes in its formation timescale. The use of U-band data significantly reduces this uncertainty, probably due to the high sensitivity of this band to the presence of recent star formation that allows to rule out instantaneous-burst solutions when recent star formation associated with larger values has effectively taken place. The use of NIR data, however, does not provide relevant information about the formation timescale of the stellar population. Moreover, the reduction achieved in the uncertainties of the different galaxy properties by using JHK data compared with those obtained using exclusively K-band data is very small (see Table 3). As we will show in Sections 4.2 & 4.3 this is not the case for the intermediate and high-redshift galaxies, where these bands now cover the redshifted optical spectrum. Finally, in the same way that the U-band, the use of UV data provides an additional reduction in the formation timescale. As it is clearly seen in Figure 2, for a particular galaxy the formation timescale is mainly degenerate with the age of the stellar population, in the sense that, within the observing errors assumed, an increase in the formation timescale accompanied by an increase in the age can result in similar UV-optical-NIR colors. Due to this age-timescale degeneracy part of the reduction in the timescale uncertainty obtained by the use of UV data can be explained by the significant reduction in the age uncertainty achieved by including UV data (see below).

4.1.2. Age

With respect to the age determination in nearby galaxies (z=0), the Figure 5a also shows that a significant reduction in the age uncertainty is achieved by including NIR data. It is important to note that the use of additional NIR data result in the same dominant degeneracy that if only optical data are used (see below), but the range of physical properties where this degeneracy takes place is significantly smaller. The most significant improvement in the age determination, however, is obtained when UV data are available. This is mainly due to the emission arising from post-AGB stars in low-metallicity populations and at ages younger than 10 Gyr and to the "UV-upturn" in high-metallicity evolved ($t > 10$ Gyr) stellar populations that result in highly peculiar UV-optical colors. However, the uncertainty in the modeling of post-AGB stars (Charlot et al. 1996) and the low-mass core helium-burning Horizontal Branch (HB hereafter) and evolved HB stars that lead to the "UV-upturn" (Yi et al. 1997), introduce additional errors in the UV-optical colors during the data-models comparison. Charlot el al. (1996) estimated using two different theoretical prescriptions that the uncertainty only in the post-AGB phase modeling could result in differences of about 1 mag in the UV-optical colors of a several-Gyr-old stellar population. Moreover, although we assumed the same observing errors for all the bands, the faint UV emission of evolved stellar populations is expected to result in very large observing errors in the UV-optical colors. Therefore, while the stellar evolution of these stars is not well understood the age determination in old stellar populations should not rely on the use of UV data.

Along with the formation timescale, the age of the stellar population in nearby galaxies is mainly degenerate with the dust extinction, in the sense that older stellar populations with low dust content have similar colors to highly-extincted, younger stellar populations. Although in the case of very old stellar populations the age-extinction degeneracy also competes with the age-metallicity degeneracy (see Worthey 1994), the age-extinction degeneracy is still dominant in this range for all the band-pass combinations and observing errors considered in this work. It could be argued that the strong discretization of the metallicity in our models could be responsible for the relatively weak age-metallicity degeneration derived. However, the fact that this behavior is observed even for the largest observing errors considered indicates that it is real and a natural consequence of the use of broad-band data. In this sense, the combination of broad-band with narrow- or medium-band data or spectroscopic indexes would break the age-extinction degeneracy, making of the age-metallicity the dominant degeneracy (see Worthey 1994).

4.1.3. Dust Extinction

The dust extinction is derived with a very high accuracy ($E(B-V)$ = 0.04–0.20 mag) even for large observing errors and relatively low number of observables (see Table 3). In the case of the nearby galaxies, the uncertainty in the dust extinction does not depend on the value of the dust extinction itself and is mainly degenerate with the age of the stellar population (see above) with some contribution from the extinction-metallicity degeneracy. In combination with BVRI optical data either the use of UV, U, or NIR data provide a significant reduction in the dust-extinction uncertainty. In order to better derive the dust extinction the use of a wider wavelength baseline in wavelength (e.g. using UVIJK) is more effective than fully covering the optical range (UBVRI). This is mainly due to the reduction in the metallicity uncertainty by the use of NIR data (see below) that leads, via the extinction-metallicity degeneracy, to a reduction in the dust-extinction uncertainty. Again, the use of JHK data instead of only K-band data do not lead to a significant reduction in the dust-extinction uncertainties.

4.1.4. Metallicity

With regard to the metallicity of the stellar population the uncertainties derived are strongly dependent on the band-pass combination available and the value of the metallicity itself. In particular, the uncertainties derived are smaller as the metallicity becomes higher (see Figure 5a). Within the age range considered, the main contributors to the optical and NIR emission of SSP galaxy are the main-sequence and RGB stars. However, for a more constant star formation, a significant contribution from core-Helium-burning stars is expected (see Charlot & Bruzual 1991). In order to determine the source of the metallicity dependence of these uncertainties we have produced the same diagrams shown in Figure 5a but restricted to formation timescales shorter than 50 Myr. The analysis of this diagram shows no dependence of the uncertainties with metallicity, which implies that the source of the dependence was the distinct photometric evolution of high-metallicity core Helium burning stars (Mowlavi et al. 1998). It is worth noting, however, that at very high metallicities the uncertainties in the modeling of the stellar populations are themselves very large because of the lack of very metal rich stars of any age in the Solar neighborhood that could be used as spectral calibrators (see Charlot et al. 1996).

The most significant reduction in the mean metallicity uncertainty is achieved when NIR data are used in combination with optical data (see Figure 5a). Although the uncertainties in the model predictions for the thermally pulsating AGB (TP-AGB hereafter) and the upper RGB can result in differences in the $(V-K)$ color predicted by different models of $\sim$0.10–0.15 mag (Charlot et al. 1996), the improvement in the metallicity determination by the use of NIR data is still relevant. In this sense, in Table 3 we show that the mean metallicity uncertainty for the U+BVRI set is 0.32 dex assuming an observing error of 0.03 mag, while the uncertainty for the U+BVRI+K set assuming an observing error of 0.10 mag is only 0.26 dex.

4.1.5. Stellar Mass

As input for the K-band mass-to-light ratio of the stellar populations we have adopted $M_{K,\odot}$ = 3.33 (Worthey 1994). It should be noticed that along with the errors in the stellar mass-to-light ratios derived here the misunderstanding of the actual IMF introduce an additional, systematic uncertainty, which, in fact, constitutes the most important source of error in the determination of the galaxy stellar mass (Bell & de Jong 2001). In addition, the poor constraints on the theoretical isochrones of upper-RGB stars and AGB stars can result in a 20 per cent uncertainty in the K-band mass-to-light ratio (Charlot et al. 1996). In Figures 6a & 6b we show the uncertainties expected in the K-band mass-to-light ratio from different sets of observables that include K-band data. These uncertainties show a strong dependence with the galaxy age and formation timescale in the sense that larger uncertainties are expected at lower values of the formation timescale and older ages. Figure 5a shows that the value of the age uncertainty (in log t scale) is almost independent of the age itself. In addition, Figure 1 indicates that the rate of change in the K-band mass-to-light ratio (with log t) is higher when the stellar population becomes older, specially for very low values of the formation timescale. Therefore, for a constant uncertainty in log t, an increase in the uncertainty of the mass-to-light ratio at very old ages is expected.

Figure 6a also shows that the mass-to-light ratio determination is biased toward lower values. This bias, which is particularly important at old ages, is probably due to the upper limit of 15 Gyr in age imposed during the data-models comparison (see Table 1), although other contributors can not be ruled out (see Sections 4.2.2 & 4.3.2). As it is clearly seen in Figure 6b, the use of UV data allows to reduce both the uncertainty and bias in the mass-to-light determination. This reduction is directly related with the reduction in the age uncertainty described above. However, as we already commented, the use of UV data for the study of stellar populations with ages older than several Gyr can lead to wrong conclusions because of the uncertain modeling of the post-AGB phase and the "UV-upturn".

The behavior described above for the timescale, age, dust extinction, metallicity, and stellar mass is identical for any observing error but with larger mean uncertainties for larger observing errors. The reader is referred to the Table 3 for the dependence of the mean uncertainties in the different galaxy properties derived with the observing errors.

4.2. Intermediate-redshift galaxies

4.2.1. Formation Timescale

In Figure 7 we show the uncertainties derived for the properties of intermediate-redshift galaxies (z=0.7). With regard to the formation timescale the uncertainties are very large (2-3 Gyr), even larger than for the nearby galaxy sample. As we commented in Section 4.1, the optical-NIR colors are quite insensitive to changes in the formation timescale with $t \ll \tau$. Therefore, since we are assuming that these galaxies are statistically younger than the those observed in our Local Universe (see Table 1) and the range in formation timescale is obviously the same, the uncertainty in the formation timescale is necessarily higher. For the same reason the uncertainty at very low timescale values is much lower than at high timescale values.

The upper panel of Figure 7a also suggests a significant bias in the timescale determination toward lower values of this property. This bias is also the consequence of the small changes in the optical-NIR colors of these galaxies with the timescale when the age is younger than the timescale value. In this case, the higher rate of change in the colors toward lower formation timescales systematically leads to lower values in order to reproduce the probability distribution associated with the observing errors. It is worth noting that, because of the reduction of this bias, the use of a larger number of bands may result in some cases in a higher timescale uncertainty (see Table 3 for the results on the U+BVRI+K and U+BVRI+JHK sets). Like in the nearby galaxies case, the dominant degeneracy involving the formation timescale is the age-timescale degeneracy, in the sense that older galaxies with high formation timescales have similar colors that younger galaxies with a more instantaneous star formation. This is true for any band-pass combination considered. With regard to the optimal set of observables, Table 3 demonstrates that for the same number of bands the use of wider wavelength baselines results in lower uncertainties. In particular, the use of the UVIJK set reduces the timescale, age, and metallicity uncertainties inherent to the UBVRI set providing also a much lower dust-extinction uncertainty than the BVRI+K set. On the other hand, the SDSS+2MASS and GALEX+SDSS+2MASS sets result in very similar uncertainties (see Table 3), which implies that the optical and NIR bands provide most of the information available in the UV and in the blue part of the optical spectrum about the galaxy age, star formation history, and metallicity.

4.2.2. Age

With respect to age of the intermediate-redshift galaxies the uncertainties derived are significantly smaller than in the nearby-galaxies case. This is mainly due to the higher rate of change in the rest-frame optical colors within the age range assumed for these galaxies compared with that assumed for the nearby galaxies (see Table 1 and Figure 1). In addition, the fact that the K-band now corresponds to the rest-frame J-band emission implies that the effect of the uncertainties in the model predictions associated with the upper RGB and AGB evolutionary stages is less important (see Section 4.4.2). On the other hand, the use of U-band data for determining ages older than 1 Gyr at these redshifts is strongly limited by the uncertainty in the modeling of the rest-frame UV emission from post-AGB stars (Charlot et al. 1996; see Section 4.1). However, the most significant decrease in the age uncertainty is achieved when NIR data are used, specially if data in all the bands (JHK) are available. This is probably due to the fact that the JHK set provides information simultaneously about the presence of AGB stars (via the rest-frame z' and J bands) and main-sequence stars (via the rest-frame R-band).

Figure 5a also shows the existence of a significant bias toward younger ages for the BVRI and UBVRI sets. In this case the presence of this bias is due (1) to the existence of a formation timescale bias and a strong age-timescale degeneracy and (2) to the fact that the optical colors of the stellar populations change more slowly as the population becomes older. In the latter case, in order to reproduce the distribution of optical colors associated with the observing errors, the best-fitting solution should be found at younger ages, where the intrinsic dispersion of the model colors is larger. As we show below a bias in age also results in a bias in the galaxy K-band mass-to-light ratio. The use of wider wavelength baselines allows to significantly reduce this bias. In particular, the use of the UVIJK leads to a less severe bias and lower age uncertainties than the U+BVRI and the U+BVRI+K sets. Within the age uncertainty interval the degeneracy is mainly dominated by the age-timescale degeneracy with some contribution from the age-extinction degeneracy in those band-pass combinations that do not include UV or U-band data.

4.2.3. Dust Extinction

The dust extinction in the sample of intermediate-redshift galaxies is derived with high accuracy, specially when U-band data are available (see Figure 7a). In this case, the uncertainties expected in $E(B-V)$ are in any case smaller than 0.10 mag for observing uncertainties as high as C_n = 0.10 mag. The significant reduction achieved, if we compare these results with those derived for the nearby galaxies, is due to the very high sensitivity of the redshifted UV emission to the presence of small amounts of dust. In those band-pass combinations not including U-band data we notice a clear dependence of the dust-extinction uncertainty with the value of the extinction itself, with larger uncertainties at larger values of the extinction (see Figure 7a). The analysis of the PCA1 components also indicates that at dust-extinction values higher than $E(B-V) > 0.5$ mag the age-extinction degeneracy becomes very important. This implies that in highly extincted intermediate-redshift galaxies a small increase in the amount of dust can lead to the same optical colors (specially if U-band data are not used) that a comparable decrease in the age of the stellar population would produce.

4.2.4. Metallicity

With regard to the metallicity uncertainty, Figure 7a shows that the uncertainty decreases with the value of the metallicity itself. The reduction is particularly important when NIR data are available. The use of the three JHK NIR bands reduces this uncertainty over the whole range of metallicities. In this sense, the use of the UVIJK set results in lower metallicity uncertainties than the U+BVRI and the U+BVRI+K sets (see Table 3). It is important to keep in mind that the JHK filters now cover the rest-frame R, z^0, and J bands. In the age range considered the main contribution to the rest-frame optical emission comes from main-sequence stars. On the other hand, the rest-frame NIR emission, along with main-sequence stars, shows an important contribution from AGB and core-Helium-burning stars (see Charlot & Bruzual 1991). The role played by AGB stars is more relevant if the formation is instantaneous, while the core-Helium-burning stars may dominate the total NIR emission for a more constant star formation scenario. Therefore, the behavior described above is probably due to the distinct evolution of high-metallicity AGB stars (see Willson 2000 and references therein) and core-Helium-burning stars (Mowlavi et al. 1998) compared with the relatively well-defined sequence in their evolutionary properties established for sub-solar metallicities. Within the error intervals derived, the metallicity is mainly degenerate with the age, specially in those sets including U-band data. This is probably due to the reduction in the age-extinction degeneracy thanks to the information provided by the U-band data about the rest-frame UV.

4.2.5. Stellar Mass

The comparison between Figures 6b and 7b shows that the mean uncertainties in the K-band mass-to-light ratio (or stellar mass) of intermediate-redshift galaxies are much lower than those derived for the nearby sample. First, it is important to note that in these figures we represent absolute errors. For a Solar-abundant 12 Gyr-old nearby galaxy formed instantaneously the K-band mass-to-light ratio is 1.3 $M_\odot/L_{K,\odot}$, while for a 5 Gyr-old galaxy at z=0.7 is 0.4 $M_\odot/L_{K,\odot}$. Therefore, the relative uncertainties, assuming the average absolute uncertainties given in Table 3 for C_n = 0.07 mag, would be about 30 and 20 per cent, respectively for the nearby and intermediate-redshift galaxies. Although this still implies a significant improvement in the K-band mass-to-light ratio determination, it is also noticeable that the K filter now traces the rest-frame J-band luminosity, which is more affected by the misunderstanding about the actual IMF (see Bell & de Jong 2001). Finally, the J-band luminosity is also more sensitive to small differences between the assumed exponential star formation and the galaxy actual star formation history than the rest-frame K-band data.

As we pointed out in Section 4.2.2 the bias in the age determination toward lower age values also leads to a strong bias in the K-band mass-to-light ratio of intermediate-redshift galaxies due to the systemic decrease in the rest-frame J-band luminosity per Solar mass with the age of stellar population when the age is older than 1 Gyr.

4.3. High-redshift galaxies

4.3.1. Formation Timescale

With regard to the formation timescale, Figure 8a shows that the bias toward lower timescale values observed at intermediate redshift is even more pronounced at high-redshift. This bias is a natural consequence of the difficulty of deriving/predicting the long-term star formation history of a galaxy when it is still very young. This is also evidenced by the fact that the mean timescale uncertainty increases systematically with redshift for the same observing errors and band-pass combinations. In Table 3 we also show that in many cases (BVRI vs: U+BVRI; SDSS vs: SDSS+2MASS) the mean timescale uncertainties increase when a larger number of observing bands is used, with a progressive reduction in this bias. As in the intermediate-redshift case the dominant degeneracy involving the galaxy formation timescale occurs with the age of the stellar population.

4.3.2. Age

The large formation timescale uncertainty described above and the existence of a strong age-timescale degeneracy, specially at ages older than 100 Myr, lead to very large age uncertainties, even larger than those derived for the intermediate-redshift galaxies. The age-timescale degeneracy at ages younger than 100 Myr is significantly smaller because at these young ages a change in the formation timescale, which ranges between 200 Myr–6 Gyr (see Table 1), does not affect to the UV-optical-NIR colors of the stellar population. In other words, the degeneracy in timescale within this age range is complete and no correlation between the age uncertainty and any other uncertainty is expected. In this case the main degeneracies are the age-extinction and the age-metallicity ones.

Moreover, the age-timescale degeneracy in combination with the bias in formation timescale described above are also responsible for the strong bias in age observed in Figure 8a at ages older than 50 Myr. The fact that the UVIJK set provides a better age and timescale determination than the U+BVRI and U+BVRI+K sets demonstrates the importance of obtaining JHK data in order to derive the properties of high-redshift galaxies. This is due to the fact that the JHK filters now cover the rest-frame V, R, and z' optical bands, where the changes due to galaxy evolution are more noteworthy and the information content about the galaxy properties is larger. In particular, the JHK filters would provide information simultaneously about the presence of main-sequence stars (via the rest-frame V and R bands), core-Helium-burning stars (via the rest-frame V, R, and z' bands), and AGB stars (via the rest-frame z'-band; $t>0.5$ Gyr).

4.3.3. Dust Extinction

Because of the extensive coverage of the UV range of the spectrum, the study of high-redshift galaxies using optical-NIR colors leads to very small dust-extinction uncertainties. In this sense, the dust-extinction uncertainties given in Table 3 at this redshift assuming an observing error of 0.10 mag are in the range $E(B-V)$ = 0.03–0.07 mag. The dust extinction within the interval of uncertainty is mainly degenerate with the age of the stellar population.

4.3.4. Metallicity

Figure 8 shows that the metallicity uncertainty for the high-redshift sample does not show the strong metallicity dependence found in nearby and intermediate-redshift samples. Only when JHK NIR data are available the uncertainties at very high metallicities become significantly smaller than those derived for the low metallicity galaxies. As we commented in Section 4.2.4 for the intermediate-redshift case, this is probably due to the distinct signature of high-metallicity core-Helium-burning stars (eg: in the number ratio of blue-to-red supergiants; Mowlavi et al. 1998) within the age range considered. In the case of a SSP galaxy, these stars dominate the rest-frame VRz' (JHK at $z=1.4$) emission for ages younger than 0.4 Gyr, while the emission at shorter wavelengths comes mainly from main-sequence stars (see Charlot & Bruzual 1991). It is important to note that the core-Helium-burning stars may dominate the emission in the R and z' bands up to ages of 5 Gyr for larger formation timescales. Within the uncertainty intervals obtained, the metallicity is mainly degenerate with the age of the stellar population.

4.3.5. Stellar Mass

The K-band mass-to-light ratio uncertainties derived here are very small compared with those obtained from the nearby and intermediate-redshift samples, with values ranging between 0.01 and 0.06 $M_{\odot}/L_{K,\odot}$. If we adopt a K-band mass-to-light of 0.27 $M_{\odot}/L_{K,\odot}$, which corresponds to the value expected for a 3 Gyr-old galaxy with Solar metallicity, the relative uncertainty would range between 5% and 20%, depending of the band-pass combination available. Figure 8b shows that there is also a strong dependence of the mass-to-light ratio uncertainty with the value of the mass-to-light ratio itself. In particular, a clear minimum in its uncertainty is observed at ages older than 8 Myr, which is probably associated with the evolution of the massive stars off the main sequence toward the red supergiant phase. During this part of the evolution a sudden change in the rest-frame z' luminosity and optical colors of a SSP is produced, which could explain why the uncertainty is particularly small around this age value.

4.4. Effects of the Model Uncertainties

In this section we analyze the results obtained when the optical-NIR colors of a sample of galaxies generated using the GISSEL99 models are compared with the predictions of the PEGASE evolutionary synthesis models. We have restricted this comparison to the nearby sample and the range of properties specified in Table 1. The results of this comparison are shown in Figure 9.

4.4.1. Formation Timescale

Figure 9a shows that the same bias toward lower values of the formation timescale that we noted for the intermediate and high-redshift samples is also present in this case (see Sections 4.2.1 & 4.3.1). The main reason for the existence of this bias is the small change in the optical-NIR colors of the stellar population with the timescale when the age $t \ll \tau$. Therefore, in order to compensate both the observing errors and the differences in the color predictions between the GISSEL99 and PEGASE models, the best-fitting solution has to be found at lower values of the timescale where the intrinsic dispersion of the colors is larger. The existence of this strong bias also leads to very small timescale uncertainties compared with those obtained using the GISSEL99 models. Within the uncertainty intervals derived, the dominant degeneracy involving the galaxy formation timescale is the age-timescale degeneracy.

4.4.2. Age

With regard to the age determination, the uncertainties derived are very similar for the BVRI and U+BVRI sets. However, for those band-pass combinations including NIR data the ages derived are strongly biased toward younger ages. The reason for this bias, which also leads to significantly smaller age uncertainties, is the offset in the $(J-H)$ and $(H-K)$ colors between the GISSEL99 and the PEGASE model predictions (see Figure 1) due to the differences in the modelling of the upper RGB and AGB phases. In particular, Figure 1b shows that the PEGASE models are ∼0.07 mag redder in $(J-H)$ and ∼0.04 mag redder in $(H-K)$ than the GISSEL99 models within the age range 4–12 Gyr. Therefore, in order to compensate for this difference in color, the best-fitting solution usually leads to younger ages, which within this age range imply bluer colors. Because the differences in the colors between the two models only occur in the NIR, the optical colors predicted by the PEGASE models at these younger ages should be bluer than those of the sample. Therefore, in order to compensate for this effect, the age bias described above has to be accompanied by strong biases in dust extinction and/or metallicity that would lead to redder optical colors. Within the error intervals derived the total degeneracy is dominated by the age-timescale and age-extinction degeneracies.

4.4.3. Dust Extinction

As we commented above (see also Figure 9a) there is a strong bias in dust extinction estimates toward higher extinction values when NIR data are used. This bias, along with the metallicity bias described in Section 4.4.4, results in a global reddening of the optical colors but a small change in the NIR colors of the galaxies in the sample. On the other hand, at very high extinction values the uncertainties are also biased by the upper limit in E(B − V) imposed during the data-models comparison procedure (see Table 1). The mean uncertainties derived, both in age, dust extinction, and metallicity are very similar to those obtained by using the GISSEL99 models.

4.4.4. Metallicity

The distribution of the uncertainty in metallicity shown in Figure 9a indicates that a strong bias toward higher metallicity values is present when NIR data are available. As we commented in Section 4.4.2, this bias is probably related with the age bias and the differences in the NIR colors predicted by the two sets of models. As in the case of GISELL 99 models, the comparison with the PEGASE models leads to a clear dependence of the uncertainty with the metallicity value itself, with smaller uncertainties at very high metallicities (see Section 4.1.4).

4.4.5. Stellar Mass

The results shown in Figure 9b with regard to the K-band mass-to-light ratios mainly reflect the biases in the galaxy property determination, with the stellar masses derived systematically smaller than the input values. This is due (1) to the bias toward younger ages described in Section 4.4.2 and (2) to the higher K-band luminosity per unit mass of the PEGASE models compared with the GISSEL99 models (see Figure 1b). Because of the stronger bias in age, the mean uncertaintines in the K-band mass-to-light ratio are smaller than those obtained using the GISSEL99 models (see Section 4.1.5). Finally, Figure 9b shows that the mass-to-light ratio uncertainty becomes higher at older ages and lower timescale values. This behavior, which is also present in the case of the GISSEL99 models (see Section 4.1.5), is due to the progressive increase in the rate of change of the K-band mass-to-light ratio with log t (see Figure 1) accompanied by a small dependence of the age uncertainty (in log t scale) with the value of the age itself.

5. CONCLUSIONS

In this study we have analyzed the dependence of the uncertainties and degeneracies in the galaxy properties upon different parameters: (1) the combination of bands available, (2) the observing errors, and (3) the galaxy properties themselves (including redshift).

Here we summarize our main results and point out some directions for the optimization of galaxy evolution studies using broad-band photometry data. We describe separately the nearby, intermediate, and high-redshift cases.

Nearby galaxies: In order to determine the star formation history, age, and dust extinction of nearby galaxies with relatively small uncertainties the use of U-band data is fundamental. The availability of K-band data also allows a reduction in the uncertainty in the age and metallicity of the stellar population, but the use of additional J and H-band data is largely redundant. The use of the K-band data is unfortunately limited by the existence of large uncertainties in the modeling of the K-band luminosities and NIR colors of stellar populations. The most significant reduction in the age and K-band mass-to-light ratio uncertainty is achieved when UV data are used. The poor treatment of the post-AGB and "extreme" HB phases by the existing evolutionary synthesis models introduce, however, an additional uncertainty during the data-model comparison, which is particularly important in the case of very old stellar populations. For the same number of observing bands, the availability of wider wavelength baselines results in lower uncertainties. Both the formation timescale and K-band mass-to-light ratio uncertainties are larger when the corresponding values for these properties are larger. On the other hand, the metallicity uncertainty decreases with the value of the metallicity itself due to the distinct photometric evolution of high-metallicity core Helium burning stars.

A complete description of the physical reasons behind these conclusions and of the degeneracies responsible for the uncertainties described above are given in Section 4.1 (see also Section 4.4).

Intermediate-redshift galaxies: The star formation history of intermediate-redshift galaxies can be derived with worse precision than in nearby galaxies because their stellar populations are younger. The age uncertainty is smaller than in the nearby-galaxies case and shows a strong bias toward younger ages. A significant reduction of this bias and of the mean uncertainties is achieved when NIR data are used, especially if all three J, H, and K-band data are available. The dust-extinction uncertainty is larger for larger values of the dust extinction itself. The use of U-band data provides an important reduction of this dependence and of the mean dust-extinction uncertainty. If U-band data are available the use of additional UV data do not provide much more information about the galaxy properties. The use of NIR data (J, H, and K-band data) significantly reduces the uncertainty in the metallicity of the galaxy. The absolute and relative uncertainties in the galaxy K-band mass-to-light ratio are smaller than those derived for nearby galaxies. However, the fact that the K filter now covers the rest-frame J-band leads to a larger uncertainty associated with the IMF and with the parameterization of the galaxy star formation history and, consequently, to a larger stellar mass uncertainty. For a more detailed description see Section 4.2.

High-redshift galaxies: As expected, the bias and mean uncertainty in the determination of the timescale for the galaxy formation are even larger in this case that in the nearby or intermediate-redshift galaxies. The age of the stellar population is derived with a large uncertainty, only reduced when JHK data are available. The dust-extinction in these galaxies can be derived to a very high accuracy even when only optical data are available. The use of JHK data is fundamental in order to improve both the age and metallicity determinations. A complete description of the uncertainties and degeneracies between these properties is given in Section 4.3.

Some of the conclusions drawn above can also be found through the literature expressed in a qualitative way. However, this work constitutes the first systematic and quantitative study on the optimization of broad-band photometry for studies on the evolution of galaxies. It is important to note that the application of these results to future galaxy surveys can help to reduce the uncertainty in the derivation of the galaxy physical properties, sometimes by weakening a particular degeneracy but most of the time by decreasing the intervals over which this degeneracy takes place. In Table 3 we have summarized the mean uncertainties in the galaxy stellar population properties derived in this paper considering different redshifts, sets of observables, and observing errors.

Our results are directly applicable to spectrophotometric surveys like the SDSS and surveys looking for emission-line galaxies at fixed redshifts (Martin, Lotz & Ferguson 2000; Moorwood, van der Werf, Cuby & Oliva 2000; Iwamuro et al. 2000; Pascual et al. 2001; Zamorano et al., in preparation). However, in the case of the blind-redshift surveys a comparison between our results and those from previous studies on the optimization of the photometric-redshifts technique (Kodama et al. 1999; Bolzonella et al. 2000; Mobasher & Mazzei 2000; Wolf et al. 2001) is still needed.

6. future applications

The results summarized above demonstrate that the design of galaxy evolution studies based only on qualitative, intuitive ideas may lead (in some cases avoidably) to large uncertainties.

Because of this we intend to apply this work to the design of future projects on galaxy evolution estimating optimal sets of observables and required signal-to-noise ratios. Although in this work we have only considered broad-band filters, this procedure is easily generalizable to combinations of broad, medium, and narrow-band filters from the far-UV to the near-infrared. In addition, the combined use of the procedure here described with state-of-the-art radiative transfer and dust models (Popescu et al. 2000) will allow us to extend this range up to sub-millimeter wavelengths.

Beyond the results shown in this paper, we can also derive, upon request, the uncertainties and degeneracies in the galaxy properties for a given combination of filters, observing errors, and galaxy redshift.

We would like to thank the referee for the useful comments and suggestions that have significantly improved the quality of this paper. We are also very grateful to A. G. Bruzual for providing the GISSEL99 evolutionary synthesis models, P. G. Pérez González, N. Cardiel and O. Pevunova for stimulating conversations, and C. Sánchez Contreras for carefully reading the manuscript and making some useful remarks. A. G. de P. acknowledges the financial support from NASA through a Long Term Space Astrophysics grant to B. F. M.

REFERENCES

Abraham, R. G., Ellis, R. S., Fabian, A. C., Tanvir, N. R., & Glazebrook, K. 1999, MNRAS, 303, 641
Aragón-Salamanca, A., Ellis, R. S., Couch, W. J., & Carter, D. 1993, MNRAS, 262, 764
Avni, Y. 1976, ApJ, 210, 642
Bell, E. F., & de Jong, R. S. 2000, MNRAS, 312, 497
Bell, E. F., & de Jong, R. S. 2001, ApJ, 520, 212
Bolzonella, M., Miralles, J.-M., Pelló, R. 2000, A&A, 363, 476.
Bressan, A., Fagotto, F., Bertelli, G., & Chiosi, C. 1993, A&AS, 100, 647
Brinchmann, J., & Ellis, R. S. 2000, MNRAS, 536, 77
Bruzual, A. G. 2000, in The Evolution of Galaxies: I-Observational Clues, ed. J. M. Vílchez, G. Stasinska & E. Pérez (Dordrecht, Germany: Kluwer Academic Publishing Company)
Bruzual, A. G., & Charlot, S. 1993, ApJ, 405, 538
Bruzual, A. G., & Charlot, S. 2001, private communication
Calzetti, D. 1997, in AIP Conf. Proc. 408, The Ultraviolet Universe at Low and High Redshift: Probing the Progress of Galaxy Evolution, ed. W. H. Waller (New York: American Institute of Physics), 403
Calzetti, D., Kinney, A. L., & Storchi-Bergmann, T. 1996, ApJ, 458, 132
Cardelli, J. A., Clayton G. C., & Mathis, J. S. 1989, ApJ, 345, 245
Cerviño, M., Luridiana, V., & Castander, F. J. 2000, A&A, 360, L5
Cerviño, M., Gómez-Flechoso, M. A., Castander, F. J., Schaerer, D., Mollá, M., Knödlseder, J., Luridiana, V. 2001, A&A, 376, 422
Charlot, S., & Longhetti, M. 2001, MNRAS, 323, 887
Charlot, S., & Bruzual, A. G. 1991, ApJ, 367, 126
Charlot, S., Worthey, G., & Bressan, A. 1996, ApJ, 457, 625
Connolly, A. J., Szalay, A. S., Dickinson M., Subbarao, M. U., & Brunner, R. J. 1997, ApJ, 476, L1
Doliber, D. L., Stock, J. M., Jelinsky, S. R., Mally, J., Jelinsky, P. N., Siegmund, O. H., & Hull, J. S. 2000, in UV, Optical, and IR Space Telescopes and Instruments, SPIE Proc., 4013, 402
Dove, J. B., Shull, J. M., & Ferrara, A. 2000, ApJ, 531, 846
Epchtein, N., et al. 1997, The Messenger, 87, 27
Ferland, G. J. 1980, PASP, 92, 596
Fioc, M., & Rocca-Volmerange, B., 1997, A&A, 326, 950
Fukugita, M., Ichikawa, T., Gunn, J. E., Doi, M., Shimasaku, K., & Schneider, D. P. 1996, AJ, 111, 1748
Gallego, J., Zamorano, J., Aragón-Salamanca, A., & Rego, M. 1995, ApJ, 455, L1
Gallego, J., Zamorano, J., Rego, M., Alonso, O., & Vitores, A. G. 1996, A&AS, 120, 323
Gil de Paz, A., Aragón-Salamanca, A., Gallego, J., Alonso-Herrero, A., Zamorano, J., & Kauffmann, G. 2000, MNRAS, 316, 357 (GIL00a)
Gil de Paz, A., Zamorano, J., Gallego, J., & Domínguez, F. de B. 2000, A&AS, 145, 377
Gil de Paz, A., Zamorano, J., & Gallego, J. 2000, A&A, 361, 465
Iwamuro, F., et al. 2000, PASJ, 52, 73
Karzas, W. J., & Latter, R. 1961, ApJS, 6, 167
Kodama, T., Bell, E. F., Bower, R. G. 1999, MNRAS, 302, 152
Krüger, H., Fritze-v Alvensleben, U., & Loose, H.-H. 1995, A&A, 303, 41
Leitherer, C., Ferguson, H. C., Heckman, T. M., & Lowenthal, J. D. 1995, ApJ, 454, L19
Leitherer, C., et al. 1999, ApJS, 123, 3
Madau, P., Ferguson, H. C., Dickinson M. E., Giavalisco M., Steidel C. C., & Fruchter, A. 1996, MNRAS, 283, 1388
Madau, P., Dickinson M. E., & Pozzeti, L. 1998, ApJ, 498, 106
Martin, P. G., & Rouleau, F. 1989, Berkeley EUV Colloq.
Martin, C., et al. 1997, American Astronomical Society Meeting, 191, # 63.04
Martin, C. L., Lotz, J., & Ferguson, H. C. 2000, ApJ, 543, 97
Mathis, J. S. 1990, ARA&A, 28, 37
Mathlin, G. P., Baker, A. C., Churches, D. K., & Edmunds, M. G. 2001, MNRAS, 321, 743
Mowlavi, N., Meynet, G., Maeder, A., Schaerer, D., & Charbonnel, C. 1998, A&A, 335, 573
Mobasher, B., & Mazzei, P. 2000, A&A, 363, 517
Moorwood, A. F. M., van der Werf, P. P., Cuby, J. G., & Oliva, E. 2000, A&A, 362, 9
Morrison, D. F. 1976, Multivariate Statistical Methods (Singapore: McGraw-Hill Book Co.)
Ortolani, S., Barbuy, B., & Bica, E. 1990, A&A, 236, 362
Osterbrook, D. E. 1989, Astrophysics of Gaseous Nebulae and Active Galactic Nuclei (Mill Valley, CA: University Science Books)
Pascual, S., Gallego, J., Aragón-Salamanca, A., Zamorano, J. 2001, A&A, in press (astro-ph/0110177)
Popescu, C. C., Misiriotis, A., Kylafis, N. D., Tuffs, R. J., & Fischera, J. 2000, A&A, 362, 138
Ronen, S., Aragón-Salamanca, A., & Lahav, O. 1999, MNRAS, 303, 284
Skrutskie, M., et al. 1997, in The Impact of Large Scale Near-IR Sky Surveys, ed. F. Garzón et al. (Dordrecht, Germany: Kluwer Academic Publishing Company), 25

Storchi-Bergmann, T., Calzetti, D., & Kinney, A. L. 1994, ApJ, 429, 572
York, D. G., et al. 2000, AJ, 120, 1579
Worthey, G. 1994, ApJS, 95, 107
Willson, L. A. 2000, ARA&A, 38, 573
Wolf, C., Meisenheimer, K., & Roser, H.-J. 2001, A&A, 365, 660
Yi, S., Demarque, P., & Oemler, A. 1997, ApJ, 486, 201
Zamorano, J., Rego, M., Gallego, J., Vitores, A. G., Gonzalez-Riestra, R., & Rodríguez-Caderot, G. 1994, ApJS, 95, 387
Zamorano, J., Gallego, J., Rego, M., Vitores, A. G., & Alonso, O. 1996, ApJS, 105, 343

Fig. 1.— Comparison of the predictions of the Bruzual & Charlot (in preparation; thick-lines), PEGASE (version 2.0; see Fioc & Rocca-Volmerange 1997; thick grey lines), and Starburst 99 (Leitherer et al. 1999; thin-lines) models for a Solar metallicity galaxy with instantaneous (SSP; panel a) and continuous star formation (panel b).

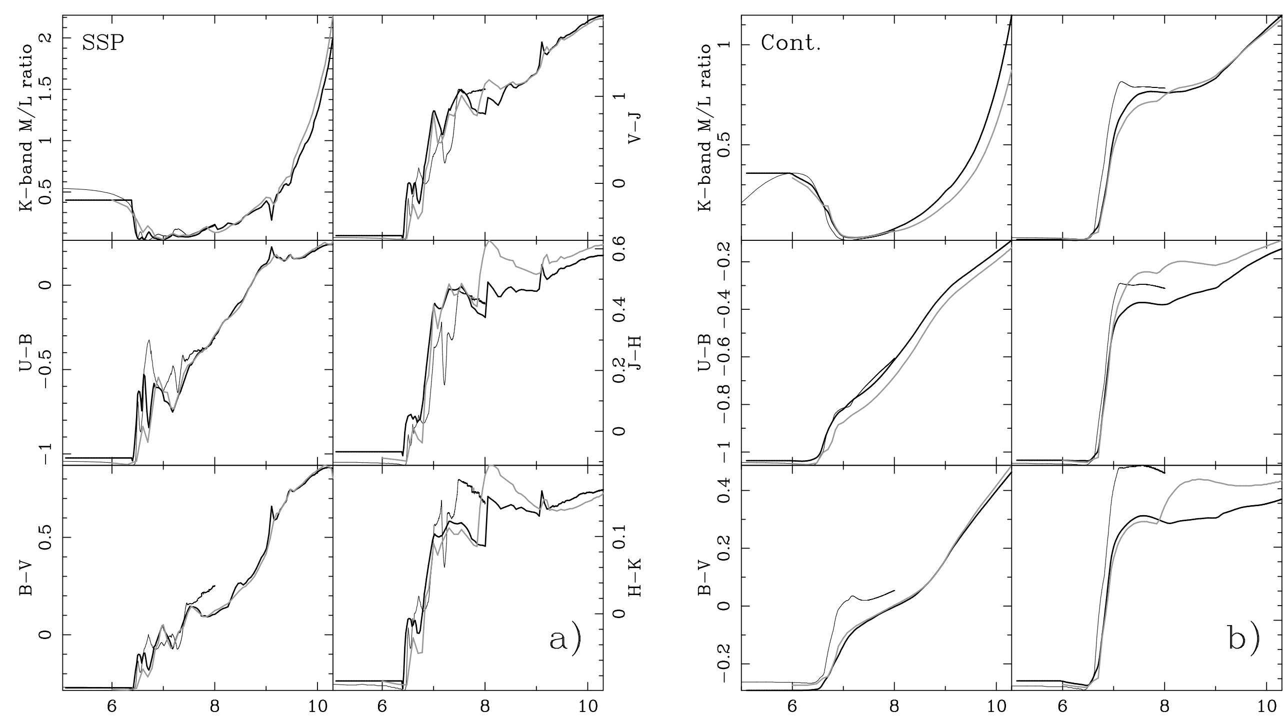

Fig. 2.— a, b & c) Top panels: Distribution of solutions associated with the 200 Monte Carlo simulations in the timescale-age space for a nearby galaxy with a formation timescale of 4.5 Gyr, an age of 5 Gyr, a dust extinction E(B − V) = 0.08 mag, and Solar metallicity. Middle panels: Distribution of solutions in the age-metallicity space for the same galaxy model. Bottom panels: The same for the age-extinction space. Observing errors are 0.10, 0.07, and 0.03 mag, respectively for the a, b, and c figures. The input properties of the galaxy are marked with a star symbol. This comparison was performed for the GALEX+SDSS+2MASS color set. The size of each point is proportional to the value of the maximum likelihood estimator, L, for the corresponding Monte Carlo simulation. Degeneracies between the galaxy properties are evidenced by correlations in the distribution of points.

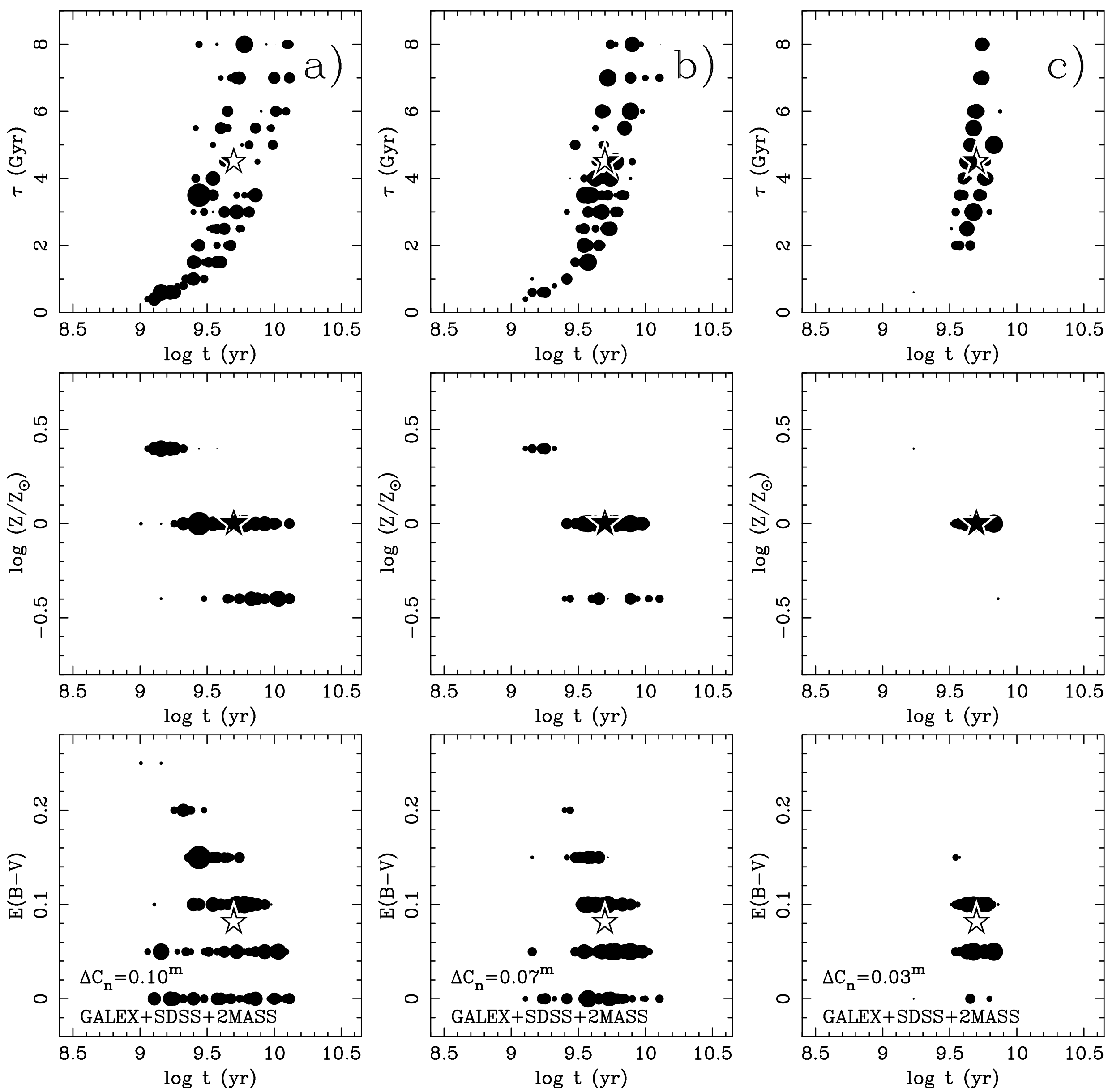

Fig. 3.— Uncertainties in the derived properties as function of the properties themselves for a subsample of 500 nearby galaxies and the U+BVRI+JHK set of observables. In Panel a the mean differences between the derived and the input properties computed in intervals of 0.5 Gyr in formation timescale, 0.025 mag in color excess, and 0.05 dex in age are represented by a light-grey line. Mean ± 1σ values for the derived properties are delimited by two dark-grey lines. The region defined by the mean ± 1σ lines is also represented in Panel b. Grey shaded areas represent the regions not covered by our comparison procedure.

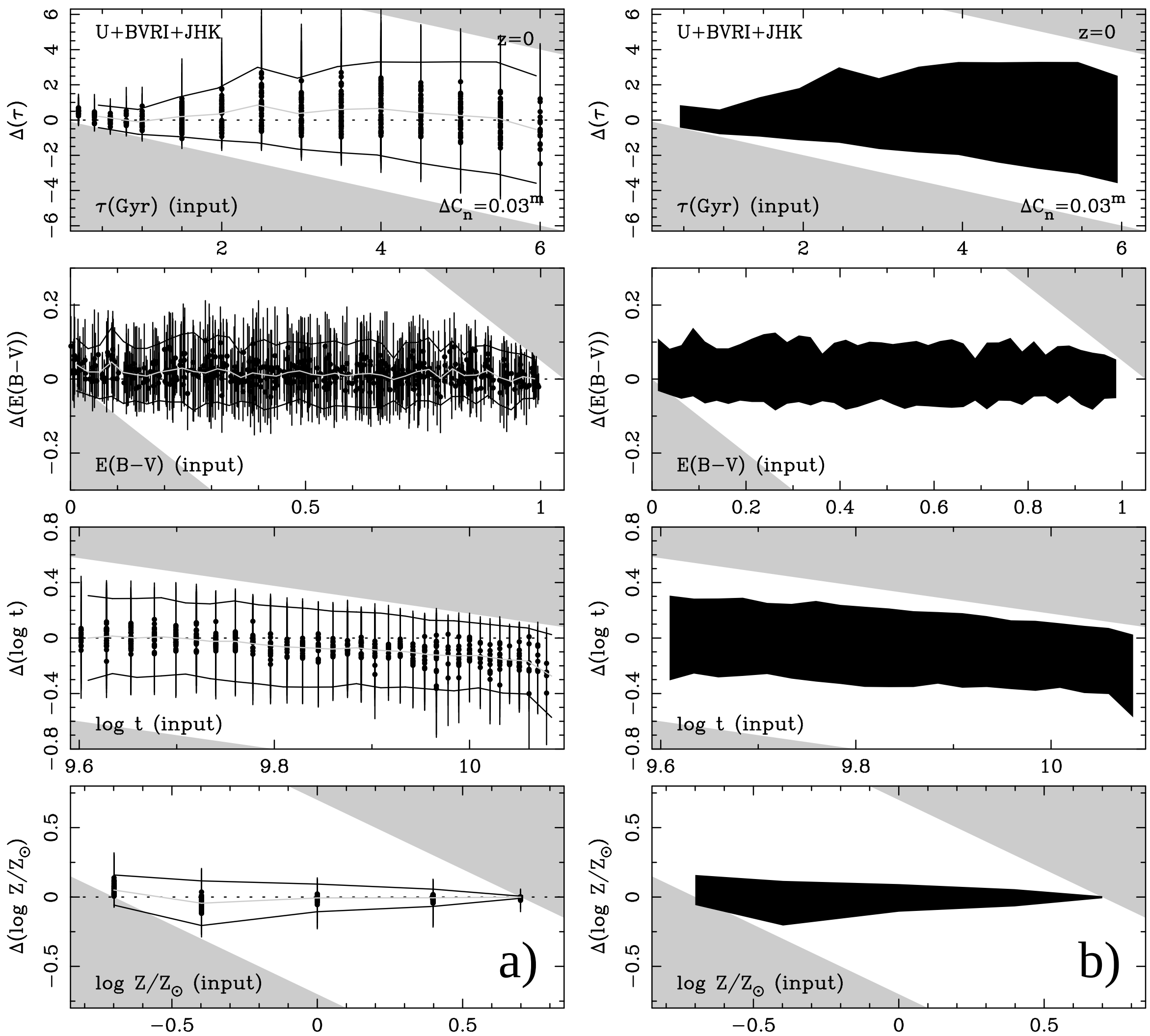

Table 1

Range in galaxy properties from which synthetic galaxy colors of the sample were generated and range in the model parameters for the data-models comparison.

	Sample	Models
$E(B-V)_{stellar}$	0.00–1.00 mag	0.00–1.05 mag
τ	0.2–6 Gyr	0.01–10 Gyr
Age (z=0)	4–12 Gyr	1–15 Gyr
(z=0.7)	1–5 Gyr	0.5–8 Gyr
(z=1.4)	3 Myr–3 Gyr	1 Myr–6 Gyr
Metallicity (Z)	0.2, 0.4, 1.0, 2.5, 5 $Z_\odot$	0.2, 0.4, 1.0, 2.5, 5 $Z_\odot$

Fig. 4.— a) Frequency histograms for the components of the PCA1 vectors for the sample of high-redshift galaxies with $\Delta C_n = 0.07$ mag for three different sets of observables (SDSS, SDSS+2MASS, and GALEX+SDSS+2MASS). This figure suggests that the age-metallicity and age-extinction degeneracies are comparable for the SDSS set, while the age-extinction and the age-timescale degeneracies are competing in the case of the SDSS+2MASS and GALEX+SDSS+2MASS sets. b) Cosine of the angle between the PCA1 vector and the age-timescale (top), age-extinction (middle), and age-metallicity (bottom) planes, as measure of the degeneracy between the stellar populations properties (see Section 4), as funcion of the age for high-redshift galaxies with an uncertainty $\Delta C_n = 0.07$ mag and the GALEX+SDSS+2MASS set. The sign of the cosine indicates if the degeneracy is in the sense that an increase in both properties can lead to the same observational properties (positive) or the value for one magnitude has to be decreased while the other is increased (negative). From this figure is clear the dependence of the dominant degeneracy with the age of the stellar population, going from the age-metallicity and age-extinction degeneracies at ages below 10 Myr, to only the age-extinction at ages between 10 Myr and 300 Myr, and the age-timescale at ages between 300 Myr and 3 Gyr (see Section 4.3.2).

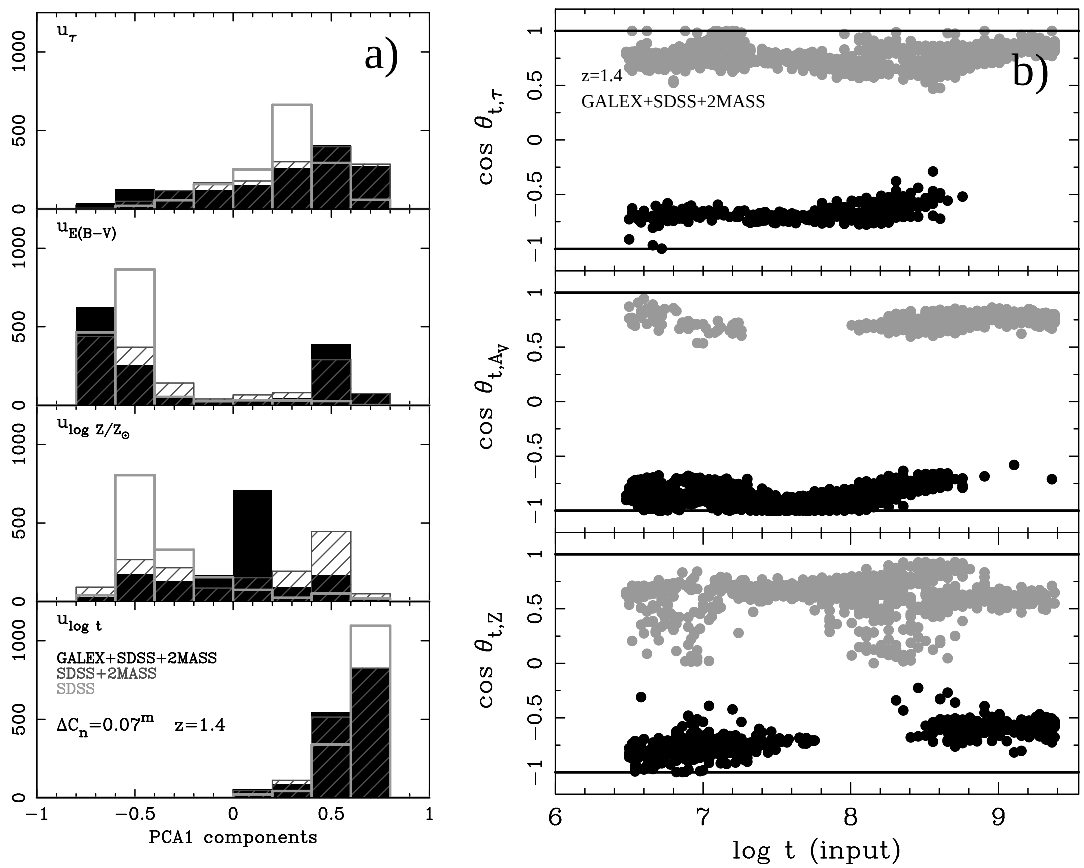

Table 2

Definition of the different combinations of filters analyzed

Bands	# of bands	Alias
$B;V;R_C;I_C$	4	BVRI
$U;B;V;R_C;I_C$	5	U+BVRI
$U;B;V;R_C;I_C;K$	6	U+BVRI+K
$U;B;V;R_C;I_C;J;H;K$	8	U+BVRI+JHK
$B;V;R_C;I_C;J;H;K$	7	BVRI+JHK
$B;V;R_C;I_C;K$	5	BVRI+K
$U;V;I_C;J;K$	5	UVIJK
$u';g';r';i';z'$	5	SDSS
$u';g';r';i';z';J;H;K$	8	SDSS+2MASS
$FUV,NUV,u';g';r';i';z';J;H;K$	10	GALEX+SDSS+2MASS

Fig. 5.| Uncertainties in the derived properties of nearby galaxies for the BVRI, U+BVRI, and U+BVRI+K sets (panel a) and the SDSS, SDSS+2MASS, and GALEX+SDSS+2MASS sets (panel b) assuming observing errors of 0.03 mag.

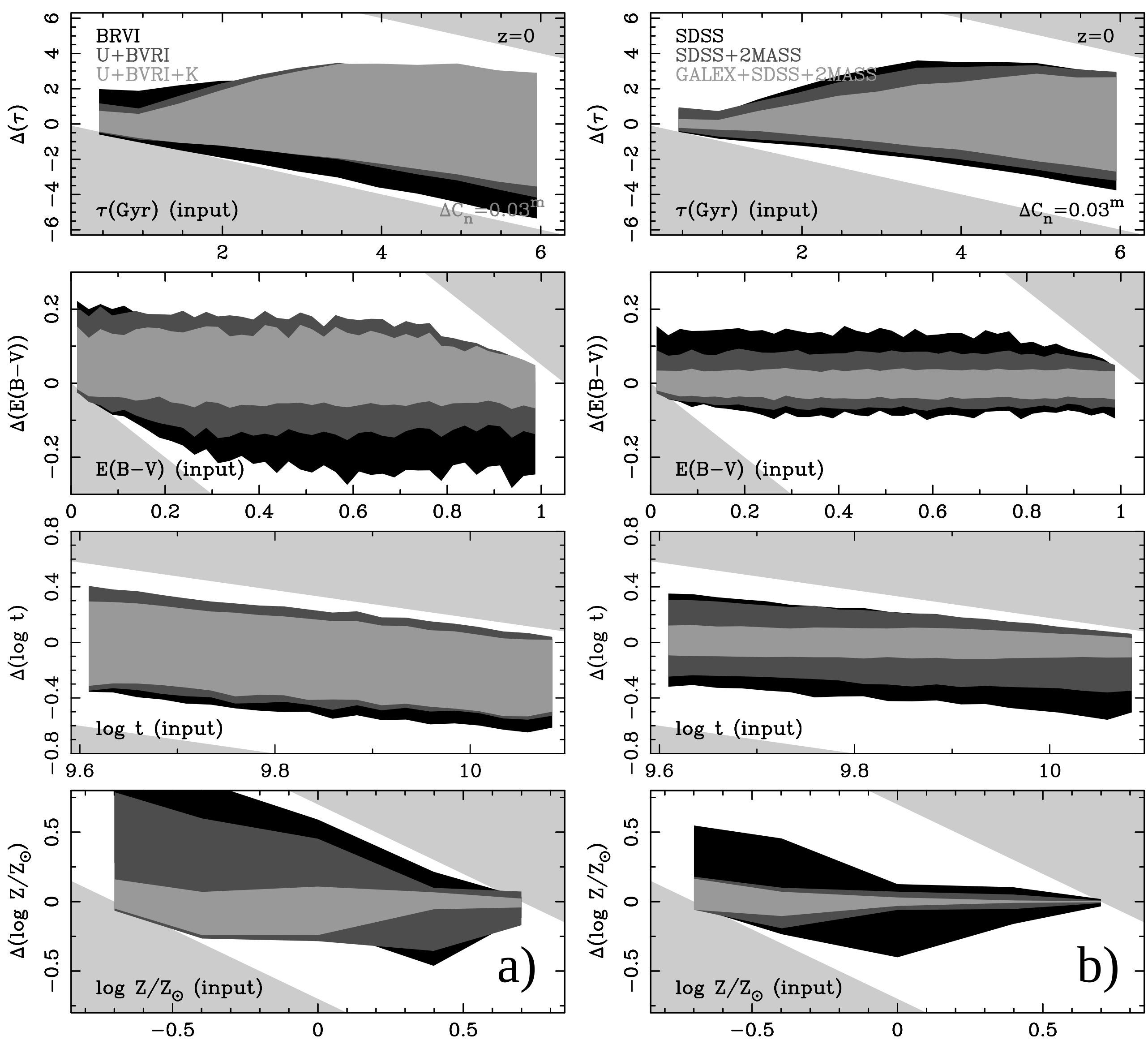

Fig. 6.— Uncertainties in the derived K-band mass-to-light ratios for the BVRI+K, U+BVRI+K, and U+BVRI+JHK sets (panel a) and the BVRI+K, SDSS+2MASS, and GALEX+SDSS+2MASS sets (panel b) assuming observing errors of 0.03 mag.

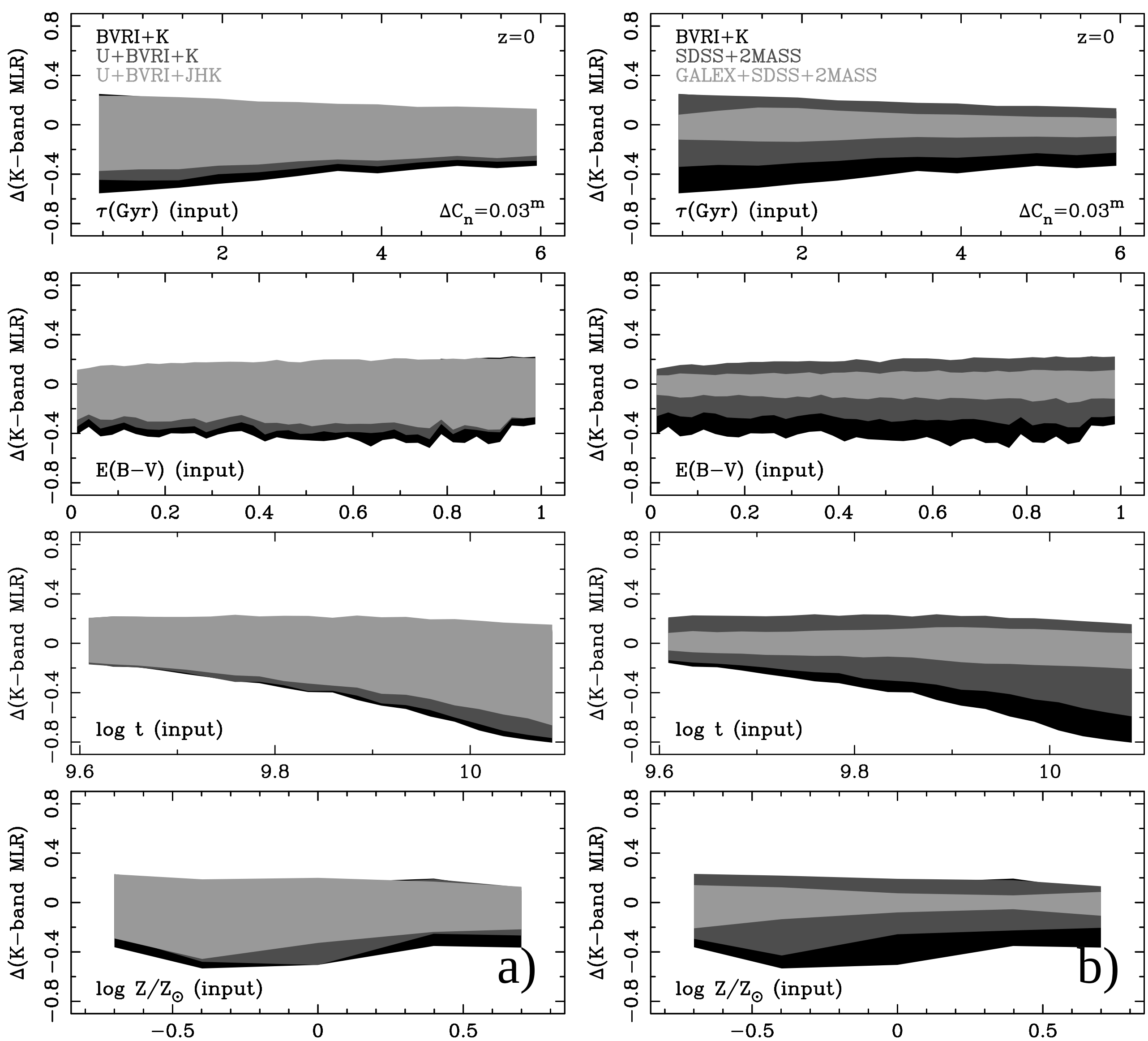

Fig. 7.— a) Uncertainties in the derived properties of intermediate-redshift galaxies for the BVRI, U+BVRI, and UBVRI+K sets assuming observing errors of 0.03 mag. b) K-band mass-to-light ratio uncertainties for the BVRI+K, U+BVRI+K, and U+BVRI+JHK sets assuming observing errors of 0.10 mag.

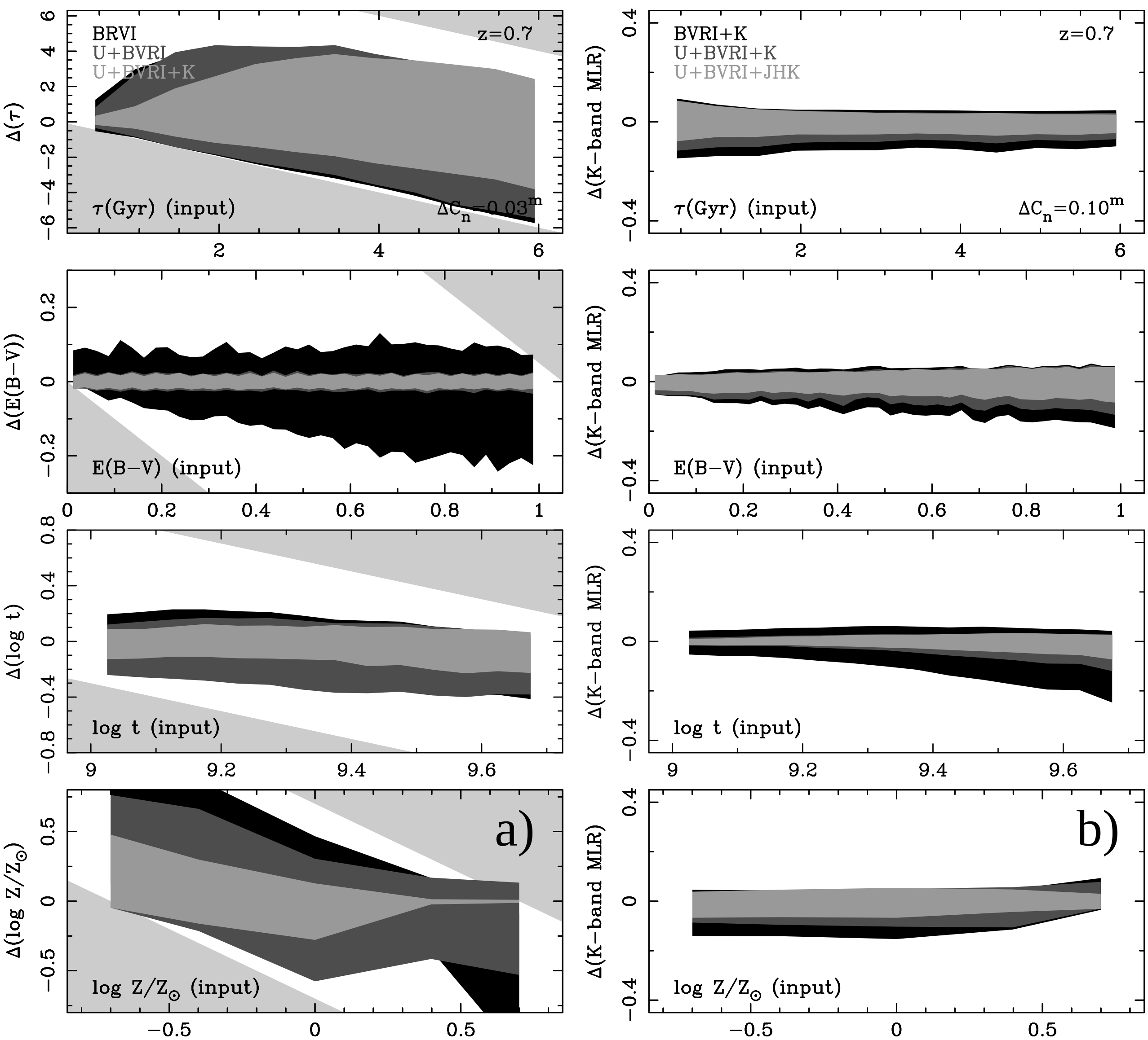

Fig. 8.— a) Uncertainties in the derived properties of high-redshift galaxies for the BVRI, U+BVRI, and UBVRI+K sets assuming observing errors of 0.03 mag. b) K-band mass-to-light ratio uncertainties for the BVRI+K, U+BVRI+K, and U+BVRI+JHK sets assuming observing errors of 0.10 mag.

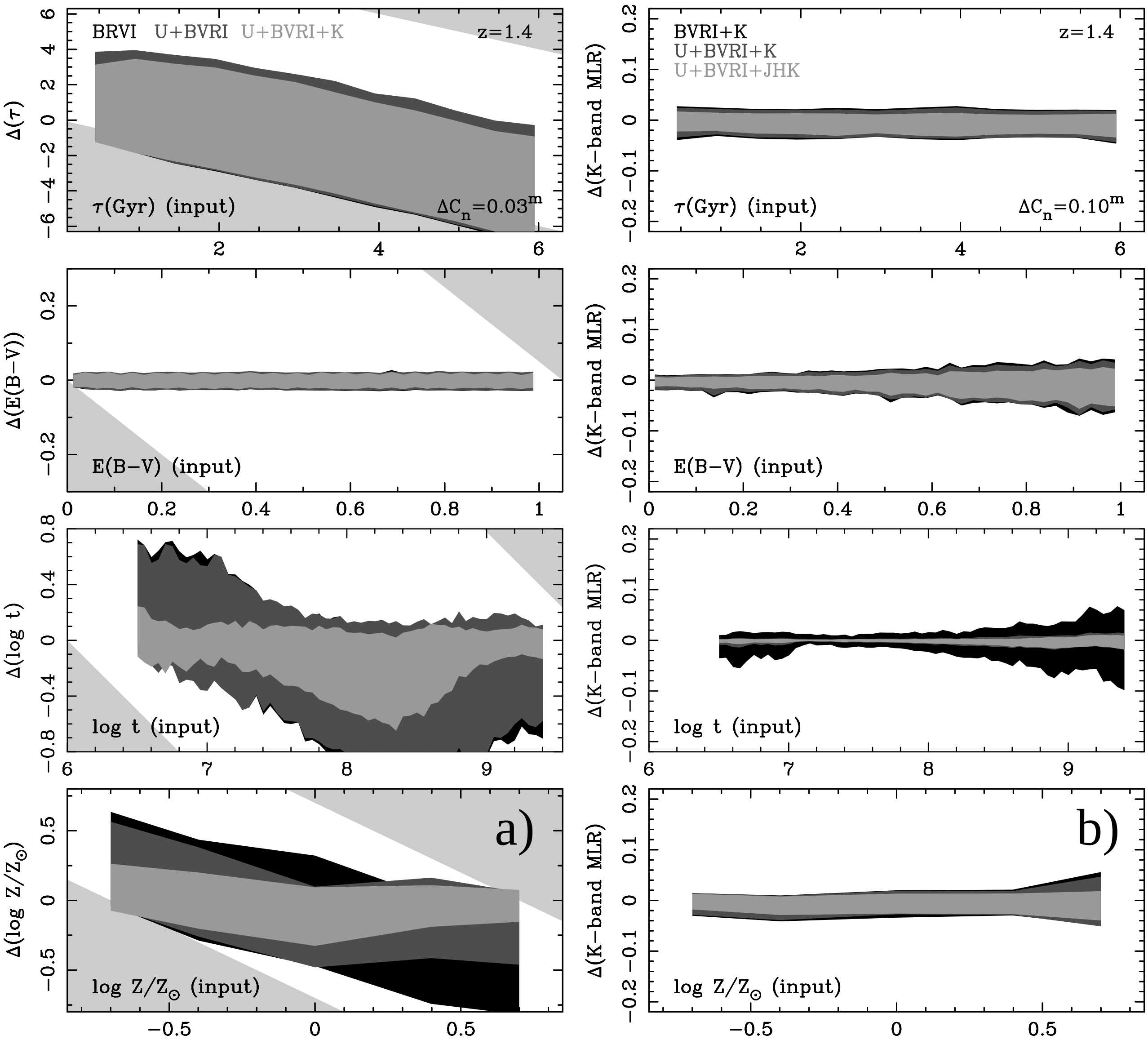

Fig. 9.— Mean timescale, age, dust extinction, metallicity (panel a), and K-band mass-to-light ratio (panel b) uncertainties derived using the PEGASE evolutionary synthesis models. In panel a we show the results for the BVRI, U+BVRI, and UBVRI+K sets, and in panel b those for the BVRI+K, U+BVRI+K, and U+BVRI+JHK sets. In both cases observing errors of 0.03 mag have been adopted.

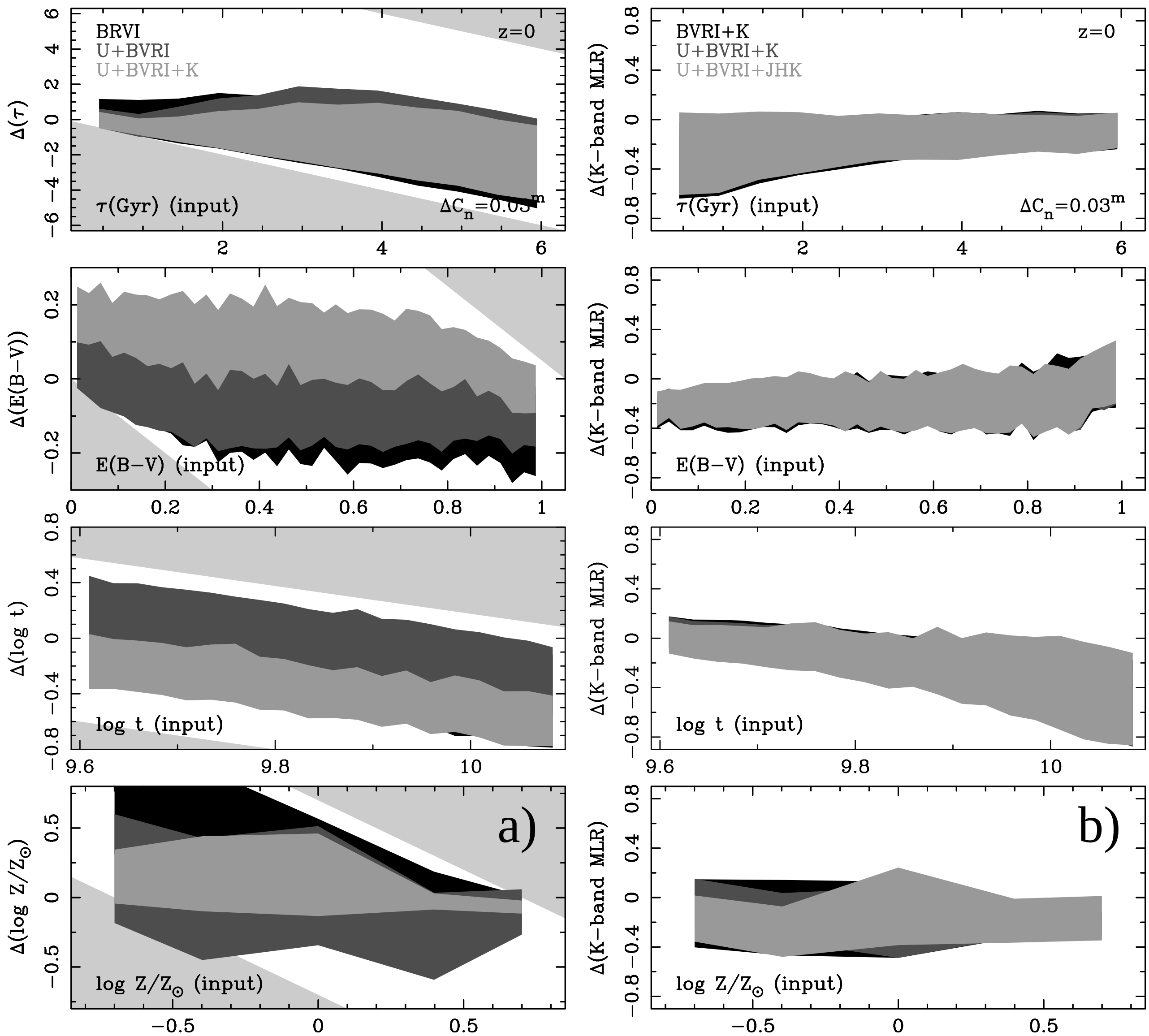

Table 3
Mean 1σ uncertainties in the derived properties

Set	Property	Unit	z=0			z=0.7			z=1.4		
		C_n (mag) =	0.03	0.07	0.10	0.03	0.07	0.10	0.03	0.07	0.10
BVRI	E(B − V)	mag	0.16	0.17	0.17	0.11	0.18	0.20	0.02	0.04	0.06
		Gyr	2.50	2.87	3.07	2.89	3.10	3.32	2.91	3.33	3.42
	log t	dex	0.36	0.37	0.38	0.23	0.31	0.35	0.45	0.71	0.84
	log Z	dex	0.33	0.33	0.33	0.44	0.46	0.45	0.37	0.45	0.48
	$(M/L)_K$	$M_\odot/L_{K,\odot}$	0.32	0.41	0.47	0.06	0.08	0.09	0.03	0.05	0.06
U+BVRI	E(B − V)	mag	0.14	0.18	0.19	0.02	0.04	0.07	0.02	0.04	0.06
		Gyr	2.27	2.69	3.00	3.10	3.10	3.11	3.11	3.34	3.33
	log t	dex	0.34	0.37	0.38	0.23	0.30	0.34	0.45	0.68	0.81
	log Z	dex	0.32	0.41	0.45	0.38	0.51	0.54	0.29	0.37	0.38
	$(M/L)_K$	$M_\odot/L_{K,\odot}$	0.32	0.41	0.47	0.05	0.08	0.09	0.03	0.05	0.06
U+BVRI+K	E(B − V)	mag	0.09	0.14	0.17	0.02	0.04	0.05	0.02	0.04	0.05
		Gyr	2.19	2.75	3.03	2.29	2.95	3.19	2.79	3.00	3.08
	log t	dex	0.28	0.35	0.38	0.13	0.21	0.24	0.20	0.28	0.33
	log Z	dex	0.11	0.20	0.26	0.15	0.22	0.26	0.17	0.29	0.34
	$(M/L)_K$	$M_\odot/L_{K,\odot}$	0.26	0.33	0.35	0.03	0.06	0.06	0.01	0.02	0.03
U+BVRI+JHK	E(B − V)	mag	0.08	0.14	0.17	0.02	0.03	0.05	0.02	0.03	0.04
		Gyr	2.12	2.70	2.96	2.35	3.07	3.35	3.19	3.44	3.44
	log t	dex	0.26	0.36	0.39	0.09	0.17	0.22	0.12	0.23	0.29
	log Z	dex	0.09	0.20	0.26	0.10	0.17	0.22	0.06	0.17	0.23
	$(M/L)_K$	$M_\odot/L_{K,\odot}$	0.24	0.35	0.37	0.02	0.04	0.05	0.01	0.01	0.02
BVRI+JHK	E(B − V)	mag	0.10	0.17	0.18	0.04	0.10	0.13	0.02	0.03	0.05
		Gyr	2.53	2.97	3.14	2.38	3.08	3.30	3.22	3.47	3.45
	log t	dex	0.32	0.38	0.40	0.12	0.22	0.28	0.13	0.24	0.29
	log Z	dex	0.13	0.23	0.28	0.11	0.20	0.25	0.07	0.19	0.25
	$(M/L)_K$	$M_\odot/L_{K,\odot}$	0.29	0.37	0.39	0.03	0.05	0.06	0.01	0.02	0.02
BVRI+K	E(B − V)	mag	0.12	0.17	0.18	0.08	0.14	0.16	0.02	0.04	0.05
		Gyr	2.67	3.15	3.35	2.32	2.88	3.06	2.72	2.92	3.03
	log t	dex	0.34	0.37	0.38	0.16	0.25	0.30	0.22	0.30	0.34
	log Z	dex	0.15	0.23	0.28	0.20	0.29	0.31	0.26	0.39	0.44
	$(M/L)_K$	$M_\odot/L_{K,\odot}$	0.30	0.34	0.36	0.05	0.08	0.09	0.02	0.03	0.03
UVIJK	E(B − V)	mag	0.10	0.16	0.19	0.02	0.04	0.07	0.02	0.03	0.05
		Gyr	2.33	2.87	3.14	2.54	3.21	3.49	3.14	3.41	3.42
	log t	dex	0.30	0.36	0.38	0.11	0.18	0.23	0.16	0.27	0.33
	log Z	dex	0.13	0.24	0.29	0.11	0.18	0.23	0.08	0.19	0.24
	$(M/L)_K$	$M_\odot/L_{K,\odot}$	0.29	0.36	0.38	0.02	0.04	0.05	0.01	0.02	0.02
SDSS	E(B − V)	mag	0.10	0.14	0.17	0.02	0.06	0.09	0.03	0.05	0.07
		Gyr	2.28	2.73	2.93	2.93	3.11	3.23	2.94	3.05	2.97
	log t	dex	0.31	0.39	0.41	0.18	0.26	0.31	0.39	0.61	0.74
	log Z	dex	0.21	0.31	0.35	0.40	0.44	0.45	0.25	0.32	0.37
	$(M/L)_K$	$M_\odot/L_{K,\odot}$	0.30	0.38	0.40	0.04	0.06	0.08	0.02	0.04	0.05
SDSS+2MASS	E(B − V)	mag	0.07	0.14	0.16	0.02	0.04	0.05	0.02	0.03	0.04
		Gyr	2.06	2.65	2.89	2.36	3.07	3.34	3.20	3.41	3.39
	log t	dex	0.25	0.36	0.39	0.09	0.16	0.21	0.12	0.21	0.26
	log Z	dex	0.08	0.19	0.25	0.10	0.16	0.21	0.08	0.17	0.23
	$(M/L)_K$	$M_\odot/L_{K,\odot}$	0.24	0.35	0.37	0.02	0.04	0.05	0.01	0.01	0.02
GALEX+SDSS+	E(B − V)	mag	0.04	0.09	0.12	0.01	0.02	0.02	0.01	0.02	0.03
+2MASS		Gyr	1.51	2.26	2.60	2.01	2.93	3.26	2.92	3.63	3.67
	log t	dex	0.10	0.19	0.24	0.08	0.13	0.17	0.09	0.16	0.21
	log Z	dex	0.05	0.16	0.22	0.11	0.16	0.20	0.03	0.08	0.14
	$(M/L)_K$	$M_\odot/L_{K,\odot}$	0.10	0.23	0.28	0.02	0.03	0.04	0.01	0.01	0.01